Unconstrained muscle-tendon workloops indicate resonance tuning as a mechanism for elastic limb behavior during terrestrial locomotion

Benjamin D. Robertson[1,2] and Gregory S. Sawicki

Joint Department of Biomedical Engineering, University of North Carolina-Chapel Hill and North Carolina State University, Raleigh, NC 27695

In terrestrial locomotion, there is a missing link between observed spring-like limb mechanics and the physiological systems driving their emergence. Previous modeling and experimental studies of bouncing gait (e.g., walking, running, hopping) identified muscle-tendon interactions that cycle large amounts of energy in series tendon as a source of elastic limb behavior. The neural, biomechanical, and environmental origins of these tuned mechanics, however, have remained elusive. To examine the dynamic interplay between these factors, we developed an experimental platform comprised of a feedback-controlled servo-motor coupled to a biological muscle-tendon. Our novel motor controller mimicked in vivo inertial/gravitational loading experienced by muscles during terrestrial locomotion, and rhythmic patterns of muscle activation were applied via stimulation of intact nerve. This approach was based on classical workloop studies, but avoided predetermined patterns of muscle strain and activation—constraints not imposed during real-world locomotion. Our unconstrained approach to position control allowed observation of emergent muscle-tendon mechanics resulting from dynamic interaction of neural control, active muscle, and system material/inertial properties. This study demonstrated that, despite the complex nonlinear nature of musculotendon systems, cyclic muscle contractions at the passive natural frequency of the underlying biomechanical system yielded maximal forces and fractions of mechanical work recovered from previously stored elastic energy in series-compliant tissues. By matching movement frequency to the natural frequency of the passive biomechanical system (i.e., resonance tuning), muscle-tendon interactions resulting in spring-like behavior emerged naturally, without closed-loop neural control. This conceptual framework may explain the basis for elastic limb behavior during terrestrial locomotion.

muscle-tendon mechanics | elastic limb behavior | neural control | resonance | terrestrial locomotion

Elastic limb behavior is a hallmark of terrestrial locomotion; the mechanics can be described by the physics of spring-mass interaction (1–4). Simple models that treat the entire leg as a linear spring loaded inverted pendulum (SLIP), and the body as a point mass can predict the mechanics of hopping (3), walking (4), and running (1, 4), as well as more subtle features of gait like the importance of swing-leg retraction for dynamic stability (5, 6). This simplified mechanical framework for describing whole limb behavior has led to breakthroughs in understanding of control targets in both biological locomotion (7) and bio-inspired walking robots (8, 9).

Although these mechanics are simple conceptually, understanding how they emerge from a biological limb has proven to be a far greater challenge. Every skeletal muscle exhibits nonlinear excitation-contraction coupling (10), nonlinear dependence of active muscle force on fascicle strain (11) and rate of strain (12), nonlinear force-displacement dynamics in tendon (13) and passive muscle (10), variable gearing in pennate muscle (14), variable aponeurosis stiffness (15), and history-dependent force production dynamics in both active muscle (16) and passive tendon (17).

In addition to the complicated contractile properties universal to all muscle-tendons, attachment/wrapping geometry and biological moment arms can be highly variable across the lower limb and substantially influence joint/limb level behavior and environmental interactions (18). How, then, does the underlying mechanical substrate of a limb; defined by the interaction of muscle-tendon architecture, limb morphology, and environmental/inertial demands (i.e., form) influence the neural control strategy that ultimately gives rise to simple spring-like limb behavior (i.e., function)?

Recent advances in functional imaging and instrumentation, combined with clever experimental design, have provided some insight into the role that muscle-tendon architecture and environment play in observed elastic limb-level mechanics. Perhaps due to the obvious compliance in the Achilles' tendon (19), much previous research has targeted the ankle plantar flexors as a potential source of spring-like limb behavior (20–23). Studies of both human and animal locomotion demonstrate that walking, running, and hopping all rely on tuned interactions between muscle and series tendon/aponeurosis. Utilization of series elastic tissues in this manner is thought to be responsible for a host of important outcomes, including power amplification and reduced metabolic demand in active muscle, as well as rapid response to mechanical perturbation (24, 25). The origins of these behaviors in walking and running are difficult to identify, however, as they rely on coordinated control of hip, knee, and ankle, all of which are

Significance

The fields of terrestrial biomechanics and bio-inspired robotics have identified spring-like limb mechanics as critical to stable and efficient gait. In biological systems, distal muscle groups cycling large amounts of energy in series tendons are a primary source of compliance. To investigate the origins of this behavior, we coupled a biological muscle-tendon to a feedback controlled servomotor simulating the inertial/gravitational environment of terrestrial gait. We drove this bio-robotic system via direct nerve stimulation across a range of frequencies to explore the influence of neural control on muscle-tendon interactions. This study concluded that by matching stimulation frequency to that of the passive biomechanical system, muscle-tendon interactions resulting in spring-like behavior occur naturally and do not require closed-loop neural control.

controlled by multiple uni- and biarticular muscle groups with various angles of pennation, attachment/wrapping geometries, and series compliance.

Researchers have studied mechanically simple behaviors like vertical hopping and bouncing to better understand elastic muscle-tendon interactions at the ankle joint. These stationary bouncing gaits preserve the salient features of spring-like walking and running, but minimize involvement of the knee and hip. Studies of hopping and bouncing demonstrated that muscle-tendon interaction at the ankle can be "tuned" as a function of movement frequency to cycle large amounts of energy in series elastic tissues (26–28). Tuned muscle-tendon mechanics not only resulted in spring-like joint and limb level behavior (3), but also amplified muscle-tendon mechanical power and efficiency beyond what would be possible for muscle alone (25, 29–35). The fact that hopping is primarily driven by a single muscle-tendon unit also facilitates an important conceptual bridge between whole limb behavior and classical experimental approaches to systematically probing dynamic function of individual muscles in vitro.

Studies on isolated muscles using workloop-based approaches have provided a window into the influence of neural control on dynamic muscle function (16, 36). In these experiments, cyclic limb/joint trajectories comparable to those observed in natural gait are applied by an ergometer, and the timing of muscle activation onset is varied in a controlled manner with respect to the phase of the movement cycle (29, 31, 37–39). Previous work using this technique has identified the neural stimulation timing appropriate for net zero work and large amounts of elastic energy storage and return (40). This approach is somewhat problematic, however, because in the "real-world" movement kinematics are not constrained. Instead, cyclic patterns of muscle-tendon strain are a result of the dynamic interaction between biological actuators (muscle/tendon), limb/joint architecture (transmission), and inertial-gravitational load (environment). Thus, the intricate dynamic coupling between form and function in the real world makes it difficult to gain detailed insight into how elastic limb behavior emerges under the tight kinematic constraints enforced by the classical workloop approach (41).

Understanding how interplay between neural control and the underlying structural form of the biomechanical system ultimately governs limb-level function requires a modified workloop approach constrained only by intrinsic properties of muscle/tendon, transmission, and environment. There are a select few studies that use actual inertial-gravitational loads to investigate dynamic actuation properties of skeletal muscle in single contractions. However, these studies provide little insight into the origins of cyclic steady-state behavior or the role of limb geometry in its emergence (42, 43). In recent years, advances in robotics, controls, and instrumentation have made it possible to explore the coupling between environmental dynamics and muscle-tendon architecture/limb geometry in isolated muscle experiments like never before (44, 45). A bio-robotic approach has been used in studies designed to optimize the interaction of antagonist muscle pairs for power output when working against a load of known resonant frequency (the calculation of which did not include passive muscle stiffness), as well as to identify the fundamental limits on power output imposed by muscle actuator properties and limb geometry during a single propulsive swimming stroke (46, 47). The goal of the present study was to extend the concepts put forth by previous bio-robotics studies simulating real-world loads (42, 43, 46, 48) to ask a fundamentally different question: how do the material properties of the muscle and tendon (the actuator), limb geometry (the transmission), and inertial environment (mass and gravity) ultimately govern neural control strategies that yield spring-like limb mechanics when subjected to constant gravitational force?

To establish a framework for inquiry, we start with a conceptually simple model: the driven simple harmonic oscillator (SHO). This classic mechanical system consists of a spring of known stiffness attached via rigid interface to a mass through a pulley with a fixed gear ratio. For the SHO system, a key factor governing emergent dynamics is the system natural frequency (ω_0), or the passive resonant frequency at which it will oscillate if perturbed from equilibrium in the absence of any external driving force. This frequency is determined by system mechanical parameters as follows:

$$\omega_0 = \frac{l_{in}}{l_{out}} \sqrt{\frac{k}{M}}, \qquad [1]$$

where l_{in}/l_{out} is the moment arm ratio of the spring (l_{in}) and inertial-gravitational load (l_{out}), k is passive stiffness, and M is system mass (Fig. 1A).

When driving the compliant SHO system, the relationship between the frequency of the external driving force source (ω_{Drive}) and ω_0 is critical. If ω_{Drive} is less than ω_0 the spring acts as a direct coupling between the source and the inertial-gravitational load, and their movement patterns are nearly perfectly in phase. As ω_{Drive} approaches and becomes coincident with ω_0, the phase between source and load displacement shifts, with the spring acting to decouple source and load motions while simultaneously storing and returning large amounts of elastic energy, maximizing system force and amplifying power output. If ω_{Drive} is increased beyond ω_0, phase continues to shift until source and
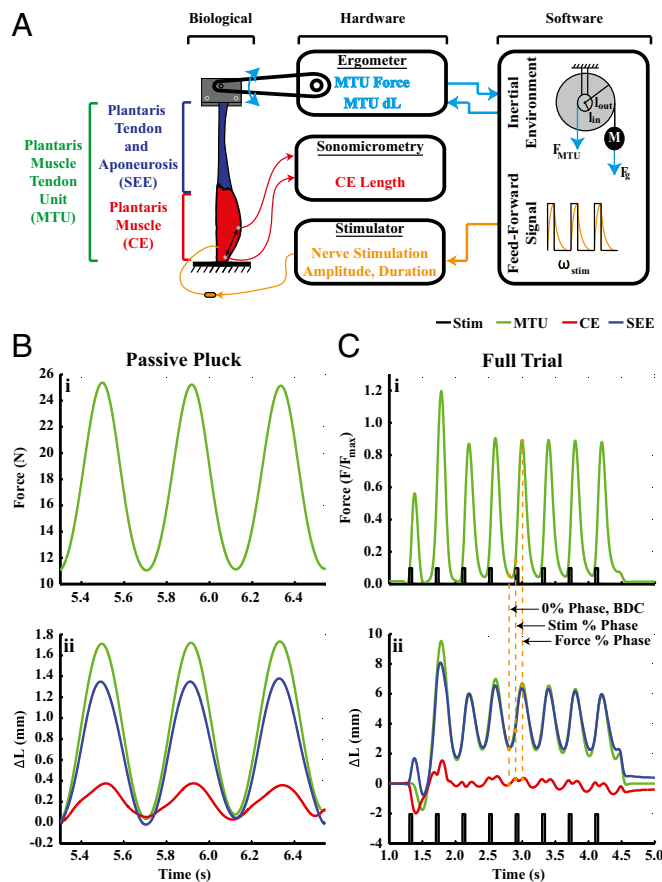
Fig. 1. (A) Schematic of bio-robotic system. (B) Force (i) and displacement (ii) data from a passive pluck condition. Note that patterns of force and displacement are cyclic. (C) Full force (i) and displacement (ii) data representative of the ω_0 condition from this study. Note that the system rapidly stabilizes and reaches steady state. The convention used to define muscle stimulation onset and peak force phase is annotated between C, i and ii.

load are perfectly out of phase, and system elastic components become a mechanical buffer that eliminates effective transmission of energy to the inertial-gravitational load (49).

Unlike the classic externally driven SHO system, force generated by a biological muscle-tendon unit (MTU) is applied internally via active muscle contraction. Active force production in a biological muscle [i.e., contractile element (CE)] exhibits nonlinear dependence on both absolute strain (11) and rate of strain (12), nonlinear excitation-contraction coupling (10), is subject to history dependent effects like work-dependent deactivation and force enhancement during lengthening (16), and can be influenced by pennation angle/variable gearing of muscle fascicles (14). Material properties of the tendon and aponeurosis [i.e., series elastic elements (SEE)] are also known to be variable, with aponeurosis stiffening due to muscle activation/deformation (15) and tendon exhibiting nonlinear stiffness at low strains, linear stiffness at high strains, and history-dependent energy dissipation over a stretch/shorten cycle (13, 17). In other words, k_{MTU} can be highly variable depending on CE active/mechanical state and SEE strain. Given all of these complicating factors, it was unclear whether a biological MTU would display a frequency dependence on both gain (i.e., force output) and phase similar to the driven SHO.

Despite these complications, a recent study that used a lumped Hill-type muscle-tendon model of human plantar flexors to drive vertical hopping indicated mechanical resonance of the muscle-tendon unit occurred when driving muscle contraction at a frequency very close to passive ω_0. That being said, Hill-type muscle-tendon models cannot reliably capture history-dependent effects like lengthening-dependent force enhancement and work-dependent deactivation in active biological muscle or hysteresis in biological tendon (16, 50–53). In an attempt to verify or refute previous simulation-based findings, as well as eliminate dependence on incomplete models of biological muscle and tendon, we (i) replaced our modeled biological MTU with a real one; (ii) simulated inertial-gravitational environment dynamics through a feedback-controlled servo-motor, which allowed closed loop dynamic interaction between the muscle-tendon unit and inertial load; and (iii) drove muscle contraction through direct nerve stimulation across a range of frequencies centered around the natural resonant frequency of the inactive muscle-tendon unit and simulated inertial load (Fig. 1A and Fig. S1).

Our central hypothesis was that form would drive function. That is, per Eq. 1, we expected that the passive natural frequency, ω_0, reflecting the combination of passive MTU stiffness (k_{MTU}), transmission geometry (l_{in}, l_{out}), and the size of the load
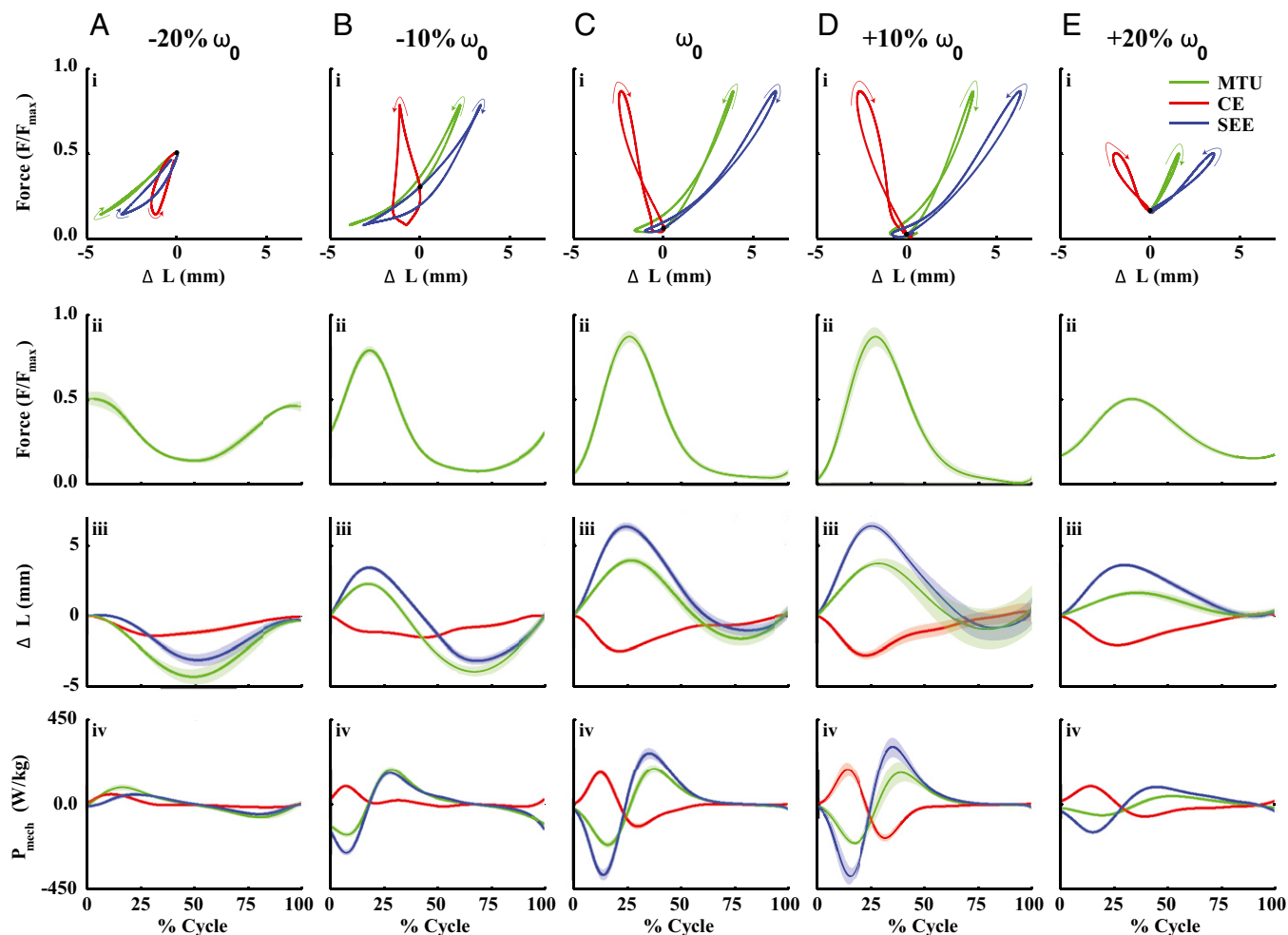

Fig. 2. A representative dataset from a single preparation showing (i) mean workloop, (ii) force ± SE, (iii) ΔL ± SE, and (iv) mechanical power ± SE output dynamics for the (A) −20%ω_0, (B) −10%ω_0, (C) ω_0, (D) +10%ω_0, and (E) +20%ω_0 conditions. All mean/SE data are based on the last four stimulation cycles from each condition. Note that SE bounds are generally small, indicating steady-state behavior from cycle to cycle. Also note progression from detuned to tuned between ω_{Drive} of −20%ω_0 and ω_0 (A, i–iv to C, i–iv), and back to detuned again in the +20% condition (C, i–iv to E, i–iv). All cycles begin (0%) and end (100%) with muscle stimulation onset.

(*M*) (i.e., form), would dictate the neural control strategy needed for spring-like behavior of the compliant MTU (i.e., function) (10). We predicted that with nerve stimulation frequency (ω_{Drive}) matched to the passive natural frequency of the mechanical system (ω_0) the MTU would resonate, exhibiting maximums in (*i*) peak force and (*ii*) elastic energy storage and return in elastic tissues (SEE). We further predicted that (*iii*) the resonant behavior would be accompanied by emergent (i.e., unconstrained) shifts in muscle stimulation phase relative to emergent cyclic MTU trajectories that are ideal for elastic energy storage/return (40).

Results

All metrics reported in tables and scatterplots are mean ($\pm$SD) for five muscle preparations across every frequency condition. For brevity, we only present overall ANOVA and least-squares regression (LSR) results (i.e., *P* values and R^2) in the text when there was a significant effect. Finer details of the analyses, including post hoc paired *t* tests and regression equations for significant effects, as well as other nonsignificant ANOVA and LSR effects, are fully documented in Table S1 (ANOVA) and Table S2 (LSR).

Overall System Dynamics. System dynamics observed in this study were generally cyclic and self-stabilizing (Fig. 1*C i* and *ii*). A representative dataset showing the mean ($\pm$SE) of the final four cycles of muscle stimulation for all muscle stimulation driving frequency (ω_{Drive}) conditions from a single experimental preparation is shown in Fig. 2. We assumed that pennation effects were small and that $F_{MTU} = F_{CE} = F_{SEE}$ (14). By examining these dynamics, it can be seen that there were alternating phases of energy storage and return at the system level (i.e., MTU) and for individual muscle and tendon/aponeurosis components (i.e., CE and SEE, respectively) of the biomechanical system over a stretch-shorten cycle (Fig. 2). Also note that, for conditions plotted against normalized cycle time (Fig. 2 *A–E, ii–iv*), deviations from mean behavior in force, length change, and power output were quite small across all conditions; (i.e., behavior is periodic and steady; Fig. 2).

MTU Peak Force and Phase Dynamics. MTU peak force varied significantly with muscle stimulation driving frequency, ω_{Drive} (ANOVA: $P = 0.032$; LSR: $P = 0.037$, $R^2 = 0.26$) and was maximized for $\omega_{Drive} \approx \omega_0$ (Fig. 3*A* and Tables S1 and S2). Maximal peak MTU force approached $0.9 \times F_{max}$ for a driving frequency of $-10\%\omega_0$, which was roughly 30% higher than values observed in the $-20\%\omega_0$ and $+20\%\omega_0$ conditions.

MTU peak force phase decreased slightly with increasing ω_{Drive} (ANOVA: $P = 0.009$; LSR: $P = 0.0002$, $R^2 = 0.47$; Fig. 3*B* and Tables S1 and S2), and consistently occurred ~50% of a cycle after minimum MTU length, or "bottom dead center" (BDC) across all conditions (Fig. 1*C, i* and *ii* and 3*B*). In contrast, muscle stimulation onset phase relative to BDC had strong dependence on driving frequency, ω_{Drive} (ANOVA: $P = 0.004$; LSR: $P = 0.012$, $R^2 = 0.46$), with a shift centered at or just above $\omega_{Drive} = \omega_0$ (Fig. 3*B* and Tables S1 and S2). For the $-20\%\omega_0$ condition, stimulation onset phase was coincident with peak force phase (50%), but transitioned to a global minimum of 25% in the ω_0 condition (Fig. 3*B*). For driving frequencies > ω_0, stimulation onset phase began to rise again, whereas peak force phase continued to drop slightly (Fig. 3*B*).

MTU Mechanical Power Output and CE, SEE Component Contributions. Elastic energy storage and return within the MTU was maximized when it was driven with muscle stimulation frequency that coincided with the natural frequency of the passive mechanical system (i.e., $\omega_{Drive} = \omega_0$). Contribution to overall mechanical power from both CE and SEE was highly dependent on driving frequency,

ω_{Drive} (ANOVA: $P < 0.0001$; LSR: $P < 0.0001$, $R^2 = 0.71$), with the SEE contributing the largest percentage (~80%) of total MTU power when $\omega_{Drive} = \omega_0$ (Fig. 3*C* and Tables S1–S3).

Average net mechanical power output ($\overline{P}_{mech}^{net}$) output of ~0 was observed across all frequencies at both the MTU (Fig. 3*D*) and component (CE/SEE) (Table S3) level, indicating steady cyclic behavior (i.e., akin to locomotion on level ground at constant speed). Net zero power output was the result of equal and maximal amounts of average positive ($\overline{P}_{mech}^{+}$) and negative ($\overline{P}_{mech}^{-}$) mechanical power from MTU and CE/SEE when $\omega_{Drive} \approx \omega_0$ (Figs. 2 *A, iv* through *E, iv* and 3*D* and Table S2).

Muscle Length and Velocity at Peak Force. The ability for the muscle (CE) to actively generate force is intrinsically coupled to its mechanical state and CE length and velocity at the time of peak force were of great interest in this study. In general, higher driving frequencies resulted in lower muscle strains at peak force (ANOVA: $P < 0.0001$; LSR: $P = 0.08$, $R^2 = 0.12$; Fig. S2*A* and Tables S1 and S2). Normalized CE velocity also depended on driving frequency, shifting from shortening at peak force, to lengthening between driving frequencies of $-10\%\omega_0$ and ω_0 (ANOVA: $P = 0.035$; LSR: $P = 0.0039$, $R^2 = 0.40$; Fig. S2*B* and Tables S1 and S2).

Modeled MTU Metabolic Rate and Apparent Efficiency. Driving the MTU near its passive natural frequency (i.e., $\omega_{Drive} \approx \omega_0$) minimized modeled average metabolic power consumption ($\overline{P}_{met}$) (Fig. S3*G*) and maximized estimated MTU apparent efficiency, ε_{app} (Fig. S3*I*). $\overline{P}_{met}$ was found to vary significantly with ω_{Drive} (ANOVA $P = 0.004$), but MTU ε_{app} did not (Table S1). Regression trends for both $\overline{P}_{met}$ and MTU ε_{app} were nonsignificant (Table S2).

Discussion and Conclusions

Overall System Dynamics. The overarching hypothesis in this study was that the form of the mechanical system, defined by the structural properties (i.e., k_{MTU}, l_{in}, l_{out}, and *M*) that determine its passive natural frequency (ω_0), would ultimately govern neural control strategies that yield proper system function (i.e., tuned spring-like MTU mechanics). Based on previous modeling studies, we expected peak mechanical tuning of biological muscle-tendon (i.e., CE/SEE) interaction, or resonance, would be observed when the system was driven with muscle stimulation at a frequency $\omega_{Drive} = \omega_0$.

Our main hypothesis was supported by experimental data demonstrating tuned MTU dynamics characteristic of mechanical resonance at a driving frequency ω_{Drive} coincident with ω_0. Peak MTU force was maximized at a frequency at or just below $\omega_{Drive} = \omega_0$ (Fig. 3*A* and Tables S1 and S2). whereas the percent contribution to overall MTU power output from energy stored/returned in SEE occurred for ω_{Drive} at or just above ω_0 (Fig. 3*C* and Tables S1 and S2). In general, maximums in both of these characteristic outcomes of a tuned MTU system appear to be centered around $\omega_{Drive} = \omega_0$.

A secondary hypothesis was that emergent muscle stimulation phase dynamics would facilitate both high peak forces and SEE energy storage and return. This prediction was also supported by experimental outcomes, as muscle stimulation onset phase shifted from ~55% in the $-20\%\omega_0$ condition to a global minimum ~25% in the $\omega_{Drive} = \omega_0$ condition (Fig. 3*B*); while peak force consistently occurred 50% of a cycle following minimum MTU length (Fig. 3*B*). This ultimately resulted in muscle activation during MTU/CE lengthening for $\omega_{Drive} > -20\%\omega_0$ (Fig. S2), which enhanced active muscle (CE) force production (Fig. 3*A*) and tendon (SEE) energy storage and return (54) (Fig. 3*C* and Table S3). These results match well with predictions from a recently published workloop study, in which a stimulation phasing of 25% relative to minimum MTU length was found to be ideal for generating net zero mechanical work and storing/returning significant amounts of energy in SEE (40). Although muscle
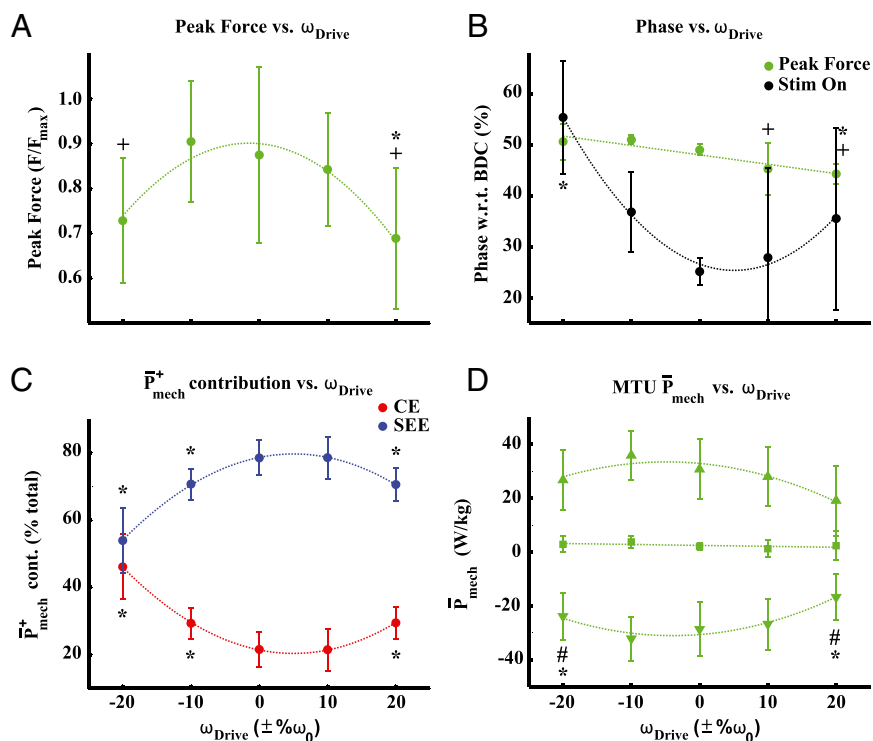
Fig. 3. Mean ± SD data for (*A*) normalized peak force, (*B*) peak force and muscle stimulation phase, (*C*) contribution of overall positive mechanical work coming from muscle (CE) vs. tendon (SEE), and (*D*) MTU positive (▲), negative (▼), and net (■) average mechanical power over a cycle of stimulation. All power values are reported in units of Watts per kilogram of muscle mass. In all figures, conditions significantly different (post hoc paired *t* test, $P < 0.05$) from ω_0 and/or the global observed maximum/minimum are indicated by a superscript of * and +/#, respectively, for these metrics.

stimulation timing dynamics (i.e., phase) were imposed in the aforementioned workloop study, here, they were an emergent property of system dynamics.

From De-Tuned to Tuned and Back Again: Frequency-Phase Coupling in Biological MTU. To provide context for the idea of resonance tuning in a biological MTU, we used the classical SHO as a behavioral template. This system is, in the mechanical sense, a grossly oversimplified representation of tuned interaction between muscle, tendon, transmission, load, and environment, but there are several fundamental features that each of these systems share.

For the classic SHO oscillator, driving it well below its resonant frequency will result in the elastic component effectively operating as a rigid coupling between the load and the driving force source. By examining the time course of the $\omega_{Drive} = -20\%\omega_0$ condition early in a stimulation cycle (the first 10–15% of the cycle following muscle stimulation onset), it can be seen that $\Delta L_{CE} = \Delta L_{MTU}$, with the preloaded tendon acting as connector between the muscle (CE) and environment/load (Fig. 2*A, iii*). In general, this is not an uncommon role for tendon to play, but is energetically not ideal for a distal MTU known to supply the majority of mechanical power output during steady locomotion from a relatively small volume of muscle (e.g., ankle plantar flexors) (30, 55). Driving the MTU at $-20\%\omega_0$ ultimately resulted in minimal values of F_{peak} (Fig. 3*A*), minimum SEE energy storage and return (Table S3), minimum SEE contributions to overall $\overline{P}_{mech}^+$ (Fig. 3*C*), maximal predicted metabolic demand (Fig. S3*G*), and minimal MTU apparent efficiency (Fig. S3*I*). Another consequence of low driving frequencies relative to ω_0 was high muscle strain, ~1.5–1.6l_0 (Fig. S2*A*), which diminished active force generation capabilities and increased force contributions from passive CE components. These high strains might be problematic for a relatively noncompliant MTU, but in vivo studies of jumping in *Rana lithobates* observed operating strains ~1.4l_o for the plantaris

muscle (56, 57). Thus, although strains observed here were high in general, they were within reason for the particular muscle group under study.

As ω_{Drive} was increased toward ω_0, the system began to tune itself much the way a SHO might. Stimulation onset occurred earlier and earlier with respect to the MTU length change cycle, and reached a global minimum at $\omega_{Drive} = \omega_0$ (Fig. 3*B*). Under these conditions, the SEE effectively decoupled CE and whole MTU length change dynamics and allowed CE to shorten internally against a lengthening SEE and MTU (Figs. 1*C i* and *ii* and 2 *B, i–E, i* and *B, iii–E, iii*). Following an initial shortening phase, the interaction of muscle mechanical state and system inertial demands was such that muscle was lengthening while operating at lower strains during the time approaching peak MTU length/force (Figs. 1*C, i* and *ii* and 2 *C, ii–E, ii* and *C, iii–E, iii* and Fig. S2 *A* and *B*). These CE strain dynamics improved active force generation capabilities due to the highly nonlinear nature of force-velocity dynamics in the neighborhood of $v_{CE} = 0$ (16). These muscle contractile conditions facilitated significant energy storage and return in the SEE (Fig. 1*C, i* and *ii*, 2, and 3*B* and Table S3), enhanced MTU mechanical power output to values above that of the muscle (CE) alone (Fig. 3*D* and Table S3), drove down predicted metabolic demand (Fig. S3*G*), and ultimately maximized MTU ε_{app} for the $\omega_{Drive} = \omega_0$ condition (Fig. S3*I*).

These highly favorable dynamics only persist for a narrow range of frequencies, however, and muscle stimulation onset phase begins to increase again for $\omega_{Drive} > \omega_0$ conditions. For the highest driving frequency examined here ($\omega_{Drive} = +20\%\omega_0$), there is still effective decoupling of CE and MTU mechanics via SEE energy storage/return, but very little of this internal energy exchange is ultimately transmitted to the load (Figs. 2*E* and 3*C*). This outcome is also consistent with SHO behavior, and the net result is reduced mechanical performance (i.e., reduced

F_{peak}, $\overline{P}_{mech}^{+/-}$) (Figs. 2E and 3 A and B), increased predicted metabolic cost (Fig. S3G), and decreased MTU ε_{app} (Fig. S3I).

Form, Function, and the Energetics of Resonance. Previous studies of human bouncing have used indirect approaches for identifying (26, 32, 58) and even imposing (59) the resonant frequency of the human ankle plantar flexor muscle-tendon complex. These studies collectively identified several key features of human bouncing at resonance, including minimal ratio of CE to whole MTU work (26, 32), maximized gain between peak force and muscle activation (59), minimized metabolic cost (32, 58), and maximized apparent efficiency (32). They did not, however, provide an explicit link between these functional features and the underlying structural characteristics of the mechanical system (i.e., form).

To begin to close the gap between mechanical resonance of a whole limb and our observation of mechanical resonance in an isolated muscle-tendon unit, we compared our bio-robotic frequency response data in this study to partially published data from human studies of hopping at frequencies from 2.2 to 3.2 Hz (Fig. S3). Joint-level and metabolic data from these studies have been published for all frequencies, whereas muscle-level data have only been published for the 2.5-Hz condition (28). For further information on collection and analysis of these data, please see Farris et al. (28, 60).

There are two distinct differences worth noting when comparing these datasets. First, the passive natural frequency of a human subject's limb is not known a priori and thus the "resonant" hopping frequency was presumed to be somewhere in the range of frequencies explored (i.e., 2.2–3.2 Hz). Second, measures of metabolic energy consumption in the human system are whole body measures rather than single muscle estimates. Although human hopping is primarily driven by the ankle joint, and it is likely that ankle energetics are driving those of the whole body, it cannot be stated definitively that all observed variation in metabolic demand was the sole result of variations in ankle MTU dynamics. Despite these differences, we found strong qualitative, if not quantitative, agreement between trends in peak MTU force (Fig. S3 A and B), MTU $\overline{P}_{mech}$ (Fig. S3 C and D), contributions of CE and SEE to MTU mechanical power output (Fig. S3 E and F), modeled/measured metabolic power (Fig. S3 G and H), and MTU apparent efficiency (Fig. S3 I and J). Based on the similarities in these trends, we feel confident that our bio-robotic framework reasonably approximates functional ankle MTU mechanics observed in human studies.

Studies of ankle-driven bouncing in humans have also demonstrated that mechanical resonance of the lumped plantar flexor MTUs is the preferred pattern of movement in a sustained (i.e., 6 min) task (58) and that inertial load and environment (e.g., added mass and increased stiffness, respectively) can influence resonant/preferential bouncing frequency (59). When resonant frequency is altered via environment perturbation, there is additional evidence indicating that proprioceptive (muscle spindle and golgi tendon) feedback allows humans to "rediscover" resonance and identify movement frequencies with optimal gain/phase relationships (59). Collectively, these studies provide compelling evidence for a default mode of operation centered on learned resonant movement frequencies that maximize efficiency/elastic energy storage and return under normal inertial conditions; and the use of a feedback-based mechanism for making adjustments in response to acute perturbations or in atypical environments (59). Outcomes reported here support this idea and demonstrate that feedback-based control is not necessary for stable and efficient MTU function when movement frequency matches that of the passive biomechanical system.

Further extending the concept of resonance tuning demonstrated here and in human studies of ankle-driven vertical hopping/bouncing (28, 55, 58, 59) to whole limb behavior during forward gait presents several formidable challenges. These include accounting for the collective behavior of additional MTUs that cross the knee and hip joints; which can alter the stiffness of the limb as a function of muscle geometry/activation, gait type, and gait speed (15, 61, 62). In addition, the center of pressure tends to shift throughout stance phase of forward gait (i.e., variable biological moment arm ratio) and there are alternating phases of single/double limb support in walking (i.e., variable load).

To our knowledge, we are the first to identify how the combination of environment dynamics and muscle/tendon actuator properties ultimately govern neural control strategies essential for stable and efficient gait. This finding was made possible by our experimental framework, which did not constrain MTU strain patterns to follow predetermined cycles, but instead allowed us to close the loop and allow dynamic mechanical interaction between the biological MTU and the physics of the environment. Our experimental apparatus enabled identification of the system-level variables that ultimately regulate emergent behavior when open-loop neural control is applied. This study demonstrated that closed-loop neural control was not required to properly time muscle activation for elastic energy storage and return. Instead, it was possible to exploit the inherent frequency phase coupling between a cyclically activated MTU and its inertial environment. Through proper selection of movement frequency alone, effective timing of muscle activation onset for maximizing MTU force and elastic energy storage and return emerged naturally. This outcome points to mechanical resonance as an underlying principle governing muscle-tendon interactions and provides a physiology-based framework for understanding how mechanically simple elastic limb behavior may emerge from a complex biological system comprised of many simultaneously tuned muscle-tendons within the lower limb (63).

Materials and Methods

Animal Subjects. All experiments shown here were approved by the North Carolina State University Institutional Animal Care and Use Committee. Five adult American bullfrogs (Lithobates catesbeianus; mean body mass = 374.3 ± 50.3 g; Table S4) were purchased from a licensed vendor (Rana Ranch) and housed in the NC State University Biological Resources Facility. On arrival, there was a 1-wk adaptation period before use in experiments. Animals were fed crickets ad libitum and housed in an aquatic environment with free access to a terrestrial platform. Before use in experiments, animals were cold-anesthetized and killed using the double-pith technique.

Surgical Protocol and Instrumentation. A single limb was detached from the killed animal at the hip joint, and the skin was removed. The limb was then submerged in a bath of oxygenated Ringers solution (100 mM NaCl, 2.5 mM KCl, 2.5 mM NaHCO₃, 1.6 mM CaCl, and 10.5 mM dextrose) at room temperature (~22 °C) for the duration of surgery. All muscles proximal to the knee, as well as the tibialis anterior, were removed with great care taken to keep the sciatic nerve intact. The plantaris longus muscle tendon unit was separated from the shank but left intact at its proximal insertion point at the knee joint. Free tendon and aponeurosis were carefully removed and preserved up to the distal insertion point at the toes. Muscles were instrumented with two sonomicrometry crystals (1 mm diameter; Sonometrics) implanted along a proximal muscle fascicle. A bipolar stimulating electrode cuff (Microprobes for Life Science) was placed around the intact sciatic nerve and connected to an Aurora 701C stimulator (Aurora Scientific). The animal's foot was removed proximal to the ankle joint, and intact portions of femur and tibia were mounted to a Plexiglas plate. A custom friction clamp was placed over distal portions of the free tendon, and the whole prep was inserted into a Plexiglas chamber with continuously circulating oxygenated ringers solution at 27 °C. The tendon clamp was then attached to a feedback controlled ergometer (Aurora 310B-LR; Aurora Scientific) for the duration of the experiment. A schematic of the experimental preparation can be seen in Fig. 1A, and a photograph of one can be seen in Fig. S1.

Determination of Muscle-Tendon Properties. To determine maximal muscle isometric force (F_{max}), the sciatic nerve was supramaximally stimulated with 0.2-ms pulses at a pulse rate of 100 Hz for 300 ms under various amounts of passive tension. The same rate and duration of stimulus pulses were used in all subsequent conditions requiring muscle activation. The condition for which F_{max} was observed was also used to approximate muscle τ_{act} and τ_{deact} values.

Using an equation from Zajac, we performed a brute force least squared error fit by sweeping a parameter space consisting of reasonable values for each time constant and determined subject-specific values for use in estimating metabolic cost ($\tau_{act} = 0.066 \pm 0.011$, $\tau_{deact} = 0.100 \pm 0.020$; Table S4) (10).

To determine the system passive resonant frequency (ω_0) for our simulated environment, we allowed the inactive MTU to oscillate against our simulated inertial system until steady-state behavior was reached (Fig. 1B). This approach provided an approximate resonant frequency and estimated linear MTU stiffness for our selected environment parameters. This observed frequency of oscillation was ω_0 ($\overline{\omega}_0 = 2.34 \pm 0.11$ Hz; Table S4), and all stimulation frequencies in dynamic conditions were centered on this value. We acknowledge that this implies a linear MTU stiffness and is only appropriate for a single set of environment parameters (e.g., mass and moment arm lengths) because it represents a local linear approximation of nonlinear MTU passive stiffness (10, 57). Furthermore, we acknowledge that, in theory, the passive muscle-tendon system should dissipate energy over a stretch-shorten cycle and exhibit decaying strain amplitude from cycle to cycle. Cyclic energy dissipation was observed initially in passive oscillations, but strain patterns eventually settled in to near constant strain amplitude (Fig. 1B). Our motor controller was imperfect, with delays between applied/measured local maximum/minimums in position (mean motor delay = 7.8 ± 0.08 ms), leading to small errors in applied vs. measured absolute motor position (mean position error = $-0.13 \pm 0.38\%$). However, these errors were small enough relative to the amplitude and time course of oscillation dynamics that we do not believe hardware/controllers to be a significant limitation. Rather, we suggest that stretch-induced calcium leakage may have played a role in active stiffening (64) and possibly limited stretch-induced membrane depolarization (65), counteracting energy dissipation known to occur in biological tissues.

Before dynamic conditions, three fixed end contractions (FECs) were performed at a stimulation frequency of ω_0 and a stimulation duty of 10% as a means of determining a baseline force for estimating muscle fatigue. This same pattern of stimulus was applied following all dynamic conditions, and if the peak force achieved was ≥60% of the initial value, the experiment was ruled a success (mean Fatigue % = $76 \pm 16.9\%$; Table S4).

Dynamic Conditions. For conditions where there was dynamic interaction between the active MTU and simulated inertial load, the driving frequency was varied between $\pm 20\%\omega_0$ in 10% intervals. The order of driving frequency conditions was randomized to counteract fatigue effects, and each frequency condition consisted of eight cycles of stimulation (Fig. 1C). Each trial began with the biological MTU under 1 N of passive tension and the inertial load resting on a virtual table. To disengage the table, MTU force must exceed that of the gravitational load

$$F_{MTU} > (l_{out}/l_{in})Mg. \quad [2]$$

Once this condition is satisfied ($F_{MTU} > 17.5$ N for parameters used here), the table is removed, and there is no constraint placed on system dynamics from that point on (Fig. 1). The system was allowed four stimulation cycles to reach steady-state behavior (Figs. 1C, 2, and 3C), and the last four cycles were used in all subsequent analysis.

Muscle-Level Mechanics. MTU force and MTU/CE ΔL were measured directly, and SEE ΔL was assumed to adhere to the following relationship:

$$\Delta L_{SEE}(t) = \Delta L_{MTU}(t) - \Delta L_{CE}(t). \quad [3]$$

MTU and component (CE/SEE) mechanical power (P_{mech}) were also computed for this preparation as follows:

$$P_{mech}(t) = F(t) \times \frac{d}{dt}L(t), \quad [4]$$

Where $F(t)$ and $L(t)$ were recorded force vs. time and length vs. time, respectively.

Determination of Phase. Phase data presented here were computed relative to the minimum MTU length observed for each stretch-shorten cycle and normalized to T_{stim} for each experimental condition. A schematic of these measured/reported values is shown in Fig. 1C. Values are reported in this manner for ready comparison with previous workloop studies where sine wave-like trajectories are applied, and stimulation phase relative to MTU oscillation period is varied systematically (40). Our study also yielded sine wave-like trajectories that had the same period as applied stimulus patterns in all frequency conditions. Stimulation phase relative to MTU strain patterns was an emergent property of system mechanics/driving frequency and was not constrained in any way as part of this study.

Average Positive Power. Average positive mechanical power ($\overline{P}_{mech}$) for MTU and CE/SEE was computed by integrating instantaneous mechanical power over a cycle and dividing by stimulation cycle period ($T_{Drive} = \omega_{Drive}^{-1}$) as follows:

$$\overline{P}_{mech} = \frac{1}{T_{Drive}} \int_{t=0}^{t=T_{Drive}} P_{mech}(t)dt. \quad [5]$$

To get average positive and negative powers ($\overline{P}_{mech}^{+}$ and $\overline{P}_{mech}^{-}$, respectively), the same calculation was made for only positive or negative regions of instantaneous power.

Modeled Metabolic Rate and Apparent Efficiency. Modeled dimensionless metabolic rate was computed as a function of normalized velocity (66), where maximal shortening velocity (v_{max}) was assumed to adhere to the relationship (67)

$$v_{max} = -13.8l_0 \times s^{-1}, \quad [6]$$

and s is the unit of time (seconds). Instantaneous dimensionless metabolic cost [$p_{met}(t)$] was scaled by physiological constant F_{max} and modeled muscle active state $\alpha(t)$ (68), which was computed using our experimentally applied stimulus pattern $u(t)$ and estimated τ_{act}/τ_{deact} values (10) (Table S4) to model instantaneous rate of metabolic power as follows:

$$P_{met}(t) = F_{max} \times \alpha[t, u(t), \tau_{act}, \tau_{deact}] \times p_{met}(t). \quad [7]$$

Average metabolic power ($\overline{P}_{met}$) was calculated using the same approach as for average mechanical power ($\overline{P}_{mech}$ in Eq. 5). To estimate CE and MTU apparent efficiency (ε_{app}) of positive mechanical work for input unit of metabolic energy, the following equation was used:

$$\varepsilon_{app} = \overline{P}_{mech}^{+} \big/ \overline{P}_{met}. \quad [8]$$

Statistical Analysis. To address our hypotheses, we conducted a one-factor, repeated-measures ANOVA (fixed effect: muscle stimulation frequency, ω_{Drive}) to test for an effect of muscle stimulation frequency on a number of key dependent measures of muscle-tendon mechanics and energetics during unconstrained workloops ($\alpha = 0.05$; JMP Pro; SAS). For dependent measures with ANOVA ($P < 0.05$), we performed post hoc Student's t tests to make pairwise comparisons of all conditions with the $\omega_{Drive} = \omega_o$ condition, as well as the study-wide maximum or minimum condition (Table S1). Finally, to establish quantitative relationships for observed trends in dependent variables as a function of muscle stimulation frequency (ω_{Drive}) we performed a least-squares regression (LSR) analysis. Each dependent variable was subjected to stepwise first- and second-order polynomial fits to all data, pooled from each experimental preparation ($n = 5$), to determine whether or not statistically significant trends were present ($P < 0.05$; Table S2). In the event that a fit was nonsignificant, the best fit based on lowest P value was used to represent observed trends. We evaluated goodness of fit using the R^2 statistic.

1. Farley CT, Glasheen J, McMahon TA (1993) Running springs: Speed and animal size. *J Exp Biol* 185:71–86.
2. Farley CT, González O (1996) Leg stiffness and stride frequency in human running. *J Biomech* 29(2):181–186.
3. Blickhan R (1989) The spring-mass model for running and hopping. *J Biomech* 22(11-12): 1217–1227.
4. Geyer H, Seyfarth A, Blickhan R (2006) Compliant leg behaviour explains basic dynamics of walking and running. *Proc Biol Sci* 273(1603):2861–2867.
5. Daley MA, Biewener AA (2006) Running over rough terrain reveals limb control for intrinsic stability. *Proc Natl Acad Sci USA* 103(42):15681–15686.
6. Seyfarth A, Geyer H, Herr H (2003) Swing-leg retraction: A simple control model for stable running. *J Exp Biol* 206(Pt 15):2547–2555.
7. Full RJ, Koditschek DE (1999) Templates and anchors: Neuromechanical hypotheses of legged locomotion on land. *J Exp Biol* 202(Pt 23):3325–3332.
8. Westervelt ER, Grizzle JW, Koditschek DE (2003) Hybrid zero dynamics of planar bipedal walkers. *IEEE-TAC* 48(1):42–56.

9. Dadashzadeh B, Vejdani HR, Hurst J (2014) *From Template to Anchor: A Novel Control Strategy for Spring-Mass Running of Bipedal Robots* (IEEE-IROS, Chicago), pp 2566–2571.
10. Zajac FE (1989) Muscle and tendon: Properties, models, scaling, and application to biomechanics and motor control. *Crit Rev Biomed Eng* 17(4):359–411.
11. Gordon AM, Huxley AF, Julian FJ (1966) The variation in isometric tension with sarcomere length in vertebrate muscle fibres. *J Physiol* 184(1):170–192.
12. Hill AV (1938) The heat of shortening and the dynamic constants of muscle. *Proc R Soc Lond B Biol Sci* 126(843):136–195.
13. Lichtwark GA, Wilson AM (2008) Optimal muscle fascicle length and tendon stiffness for maximising gastrocnemius efficiency during human walking and running. *J Theor Biol* 252(4):662–673.
14. Azizi E, Brainerd EL, Roberts TJ (2008) Variable gearing in pennate muscles. *Proc Natl Acad Sci USA* 105(5):1745–1750.
15. Azizi E, Roberts TJ (2009) Biaxial strain and variable stiffness in aponeuroses. *J Physiol* 587(Pt 17):4309–4318.
16. Josephson RK (1999) Dissecting muscle power output. *J Exp Biol* 202(Pt 23):3369–3375.
17. Maganaris CN, Paul JP (2000) Hysteresis measurements in intact human tendon. *J Biomech* 33(12):1723–1727.
18. Winters JM, Stark L (1988) Estimated mechanical properties of synergistic muscles involved in movements of a variety of human joints. *J Biomech* 21(12):1027–1041.
19. Lichtwark GA, Wilson AM (2007) Is Achilles tendon compliance optimised for maximum muscle efficiency during locomotion? *J Biomech* 40(8):1768–1775.
20. Ferris DP, Farley CT (1997) Interaction of leg stiffness and surfaces stiffness during human hopping. *J Appl Physiol (1985)* 82(1):15–22, discussion 13–14.
21. Chang YH, Roiz RA, Auyang AG (2008) Intralimb compensation strategy depends on the nature of joint perturbation in human hopping. *J Biomech* 41(9):1832–1839.
22. Farley CT, Morgenroth DC (1999) Leg stiffness primarily depends on ankle stiffness during human hopping. *J Biomech* 32(3):267–273.
23. van der Krogt MM, et al. (2009) Robust passive dynamics of the musculoskeletal system compensate for unexpected surface changes during human hopping. *J Appl Physiol (1985)* 107(3):801–808.
24. Dickinson MH, et al. (2000) How animals move: An integrative view. *Science* 288(5463):100–106.
25. Roberts TJ, Azizi E (2011) Flexible mechanisms: The diverse roles of biological springs in vertebrate movement. *J Exp Biol* 214(Pt 3):353–361.
26. Takeshita D, et al. (2006) Resonance in the human medial gastrocnemius muscle during cyclic ankle bending exercise. *J Appl Physiol (1985)* 101(1):111–118.
27. Lichtwark GA, Wilson AM (2005) In vivo mechanical properties of the human Achilles tendon during one-legged hopping. *J Exp Biol* 208(Pt 24):4715–4725.
28. Farris DJ, Robertson BD, Sawicki GS (2013) Elastic ankle exoskeletons reduce soleus muscle force but not work in human hopping. *J Appl Physiol (1985)* 115(5):579–585.
29. Lichtwark GA, Barclay CJ (2010) The influence of tendon compliance on muscle power output and efficiency during cyclic contractions. *J Exp Biol* 213(5):707–714.
30. Roberts TJ, Marsh RL, Weyand PG, Taylor CR (1997) Muscular force in running turkeys: The economy of minimizing work. *Science* 275(5303):1113–1115.
31. Lichtwark GA, Barclay CJ (2012) A compliant tendon increases fatigue resistance and net efficiency during fatiguing cyclic contractions of mouse soleus muscle. *Acta Physiol (Oxf)* 204(4):533–543.
32. Dean JC, Kuo AD (2011) Energetic costs of producing muscle work and force in a cyclical human bouncing task. *J Appl Physiol (1985)* 110(4):873–880.
33. Biewener AA, Konieczynski DD, Baudinette RV (1998) In vivo muscle force-length behavior during steady-speed hopping in tammar wallabies. *J Exp Biol* 201(Pt 11):1681–1694.
34. Biewener AA, McGowan C, Card GM, Baudinette RV (2004) Dynamics of leg muscle function in tammar wallabies (M. eugenii) during level versus incline hopping. *J Exp Biol* 207(Pt 2):211–223.
35. Biewener AA, Daley MA (2007) Unsteady locomotion: Integrating muscle function with whole body dynamics and neuromuscular control. *J Exp Biol* 210(Pt 17):2949–2960.
36. Ahn AN (2012) How muscles function–the work loop technique. *J Exp Biol* 215(Pt 7):1051–1052.
37. Barclay CJ, Lichtwark GA (2007) The mechanics of mouse skeletal muscle when shortening during relaxation. *J Biomech* 40(14):3121–3129.
38. Ettema GJ (1996) Mechanical efficiency and efficiency of storage and release of series elastic energy in skeletal muscle during stretch-shorten cycles. *J Exp Biol* 199(Pt 9):1983–1997.
39. Ettema GJ (2001) Muscle efficiency: The controversial role of elasticity and mechanical energy conversion in stretch-shortening cycles. *Eur J Appl Physiol* 85(5):457–465.
40. Sawicki GS, Robertson BD, Azizi E, Roberts TJ (2015) Timing matters: Tuning the mechanics of a muscle-tendon unit by adjusting stimulation phase during cyclic contractions [published online ahead of print July 31, 2015]. *J Exp Biol*, 10.1242/jeb.121673.
41. Marsh RL (1999) How muscles deal with real-world loads: the influence of length trajectory on muscle performance. *J Exp Biol* 202(Pt 23):3377–3385.
42. Pennycuick CJ (1964) Frog fast muscle. 3. Twitches with isometric and inertial load. *J Exp Biol* 41:273–289.
43. Baratta RV, Solomonow M, Zhou BH (1998) Frequency domain-based models of skeletal muscle. *J Electromyogr Kinesiol* 8(2):79–91.
44. Richards CT, Clemente CJ (2012) A bio-robotic platform for integrating internal and external mechanics during muscle-powered swimming. *Bioinspir Biomim* 7(1):016010.
45. Farahat W, Herr H (2005) An apparatus for characterization and control of isolated muscle. *IEEE Trans Neural Syst Rehabil Eng* 13(4):473–481.
46. Clemente CJ, Richards C (2012) Determining the influence of muscle operating length on muscle performance during frog swimming using a bio-robotic model. *Bioinspir Biomim* 7(3):036018.
47. Richards CT, Clemente CJ (2013) Built for rowing: Frog muscle is tuned to limb morphology to power swimming. *J R Soc Interface* 10(84):20130236.
48. Farahat WA, Herr HM (2010) Optimal workloop energetics of muscle-actuated systems: an impedance matching view. *PLOS Comput Biol* 6(6):e1000795.
49. Ogata K (2003) *System Dynamics* (Prentice Hall, Upper Saddle River, NJ), 4th Ed.
50. Josephson RK, Stokes DR (1999) Work-dependent deactivation of a crustacean muscle. *J Exp Biol* 202(Pt 18):2551–2565.
51. Caiozzo VJ, Baldwin KM (1997) Determinants of work produced by skeletal muscle: potential limitations of activation and relaxation. *Am J Physiol* 273(3 Pt 1):C1049–C1056.
52. Sandercock TG, Heckman CJ (1997) Force from cat soleus muscle during imposed locomotor-like movements: Experimental data versus Hill-type model predictions. *J Neurophysiol* 77(3):1538–1552.
53. Curtin NA, Gardner-Medwin AR, Woledge RC (1998) Predictions of the time course of force and power output by dogfish white muscle fibres during brief tetani. *J Exp Biol* 201(Pt 1):103–114.
54. Robertson BD, Sawicki GS (2014) Exploiting elasticity: Modeling the influence of neural control on mechanics and energetics of ankle muscle-tendons during human hopping. *J Theor Biol* 353:121–132.
55. Farris DJ, Sawicki GS (2012) The mechanics and energetics of human walking and running: a joint level perspective. *J R Soc Interface* 9(66):110–118.
56. Azizi E (2014) Locomotor function shapes the passive mechanical properties and operating lengths of muscle. *Proc Biol Sci* 281(1783):20132914.
57. Azizi E, Roberts TJ (2010) Muscle performance during frog jumping: Influence of elasticity on muscle operating lengths. *Proc Biol Sci* 277(1687):1523–1530.
58. Merritt KJ, Raburn CE, Dean JC (2012) Adaptation of the preferred human bouncing pattern toward the metabolically optimal frequency. *J Neurophysiol* 107(8):2244–2249.
59. Raburn CE, Merritt KJ, Dean JC (2011) Preferred movement patterns during a simple bouncing task. *J Exp Biol* 214(Pt 22):3768–3774.
60. Farris DJ, Sawicki GS (2012) Linking the mechanics and energetics of hopping with elastic ankle exoskeletons. *J Appl Physiol (1985)* 113(12):1862–1872.
61. Cavagna GA, Franzetti P, Heglund NC, Willems P (1988) The determinants of the step frequency in running, trotting and hopping in man and other vertebrates. *J Physiol* 399:81–92.
62. Arampatzis A, Brüggemann GP, Metzler V (1999) The effect of speed on leg stiffness and joint kinetics in human running. *J Biomech* 32(12):1349–1353.
63. NicholsT (1992) Stiffness regulation revisited. *Behav Brain Sci* 15(4):783–784.
64. Nishikawa KC, et al. (2012) Is titin a 'winding filament'? A new twist on muscle contraction. *Proc Biol Sci* 279(1730):981–990.
65. Mallouk N, Allard B (2000) Stretch-induced activation of Ca(2+)-activated K(+) channels in mouse skeletal muscle fibers. *Am J Physiol Cell Physiol* 278(3):C473–C479.
66. Alexander RM (1997) Optimum muscle design for oscillatory movements. *J Theor Biol* 184(3):253–259.
67. Sawicki GS, Sheppard P, Roberts TJ (2015) Power amplification in an isolated muscle-tendon is load dependent. *J Exp Biol*, in press.
68. Krishnaswamy P, Brown EN, Herr HM (2011) Human leg model predicts ankle muscle-tendon morphology, state, roles and energetics in walking. *PLOS Comput Biol* 7(3):e1001107.